An electrochemical cell for *in operando* ^{13}C NMR investigations of carbon dioxide/carbonate processes in aqueous solution

Sven Jovanovic[1,5], P. Philipp M. Schleker[1,3], Matthias Streun[2], Steffen Merz[1], Peter Jakes[1], Michael Schatz[1,5], Rüdiger-A. Eichel[1,4], and Josef Granwehr[1,5]

[1]Forschungszentrum Jülich, Institute of Energy and Climate Research, Fundamental Electrochemistry (IEK-9), Jülich, Germany
[2]Forschungszentrum Jülich, Central Institute of Engineering and Analytics, Electronic Systems (ZEA-2), Jülich, Germany
[3]Department of Heterogeneous Reactions, Max Planck Institute for Chemical Energy Conversion, Mülheim an der Ruhr, Germany
[4]RWTH Aachen University, Institute of Physical Chemistry, Aachen, Germany
[5]RWTH Aachen University, Institute of Technical and Macromolecular Chemistry, Aachen, Germany

Correspondence: Sven Jovanovic (s.jovanovic@fz-juelich.de)

Abstract. *In operando* NMR spectroscopy is one method for the online investigation of electrochemical systems and reactions. It allows for real-time observations of the formation of products and intermediates and it grants insights into the interactions of substrates and catalysts. An *in operando* NMR setup for the investigation of the electrolytic reduction of CO_2 at silver electrodes has been developed. The electrolysis cell consists of a three-electrode setup using a working electrode of pristine silver, a chlorinated silver wire as reference electrode and a graphite counter electrode. The setup can be adjusted for the use of different electrode materials and fits inside a 5 mm NMR tube. Additionally, a shielding setup was employed to minimize noise caused by interference of external radio frequency (RF) waves with the conductive components of the setup. The electrochemical performance of the *in operando* electrolysis setup is compared with a standard CO_2 electrolysis cell. The small cell geometry impedes the release of gaseous products and thus it is primarily suited for current densities below 1 mA/cm^2. The effect of conductive components on ^{13}C NMR experiments was studied using a CO_2 saturated solution of aqueous bicarbonate electrolyte. Despite the B_0 field distortions caused by the electrodes a proper shimming could be attained and line widths of *ca.* 1 Hz were achieved. This enables investigations in the sub-Hertz range by NMR spectroscopy. High resolution ^{13}C NMR and relaxation time measurements proved to be sensitive to changes in the sample. It was found that the dynamics of the bicarbonate electrolyte varies not only due to interactions with the silver electrode, which leads to the formation of an electrical double layer and catalyzes the exchange reaction between CO_2 and HCO_3^-, but also due to interactions with the electrochemical setup. This highlights the necessity of a step-by-step experiment design for a mechanistic understanding of processes occurring during electrochemical CO_2 reduction.

1 Introduction

The anthropologically driven atmospheric CO_2 increase is considered one of the major contributions to global warming (Hansen et al., 2008). A decline in anthropological CO_2 emissions is seen as improbable due to socio-economic factors

(Grundmann, 2016). Thus, the recycling of CO_2 by electrochemical conversion to energy-rich materials is of particular interest (Jhong et al., 2013; Whipple and Kenis, 2010; Zhu et al., 2016). One promising method in terms of cost and variability is the electrolytic reduction of CO_2, usually performed in an aqueous bicarbonate electrolyte solution (Haas et al., 2018). Depending on the metal electrode, CO_2 electrolysis yields a number of products, *e.g.* formate, hydrocarbons, alcohols and carbon monoxide (Hori, 2008; Haas et al., 2018). CO, which is a versatile educt for the chemical industry, *e.g.* as feedstock for the Fischer–Tropsch process, is obtained by using silver or gold electrodes (Hernández et al., 2017).

Despite vivid research, the reaction pathways of electrochemical CO_2 reduction are still not fully understood (Hori, 2008; Jhong et al., 2013; Kortlever et al., 2015). There are two main issues, were one originates in the complex equilibrium of CO_2 and carbonate species in aqueous systems depending on pH, temperature and partial pressure. These parameters vary with time during the electrolysis and are also a function of distance from the electrode surface (Hori, 2008). The second issue is the electrolytic CO_2 reduction which suffers further from high overpotentials, mitigated by a few selected metal catalysts. There is evidence, that the formation of an intermediate CO_2^{-} radical can cause an overpotential (Hori, 2008; Baruch et al., 2015).

To gain insights into the dynamic processes of an electrochemical system it is imperative to monitor the complete system during operation, *e.g.* using *in operando* spectroscopic techniques (Bañares, 2005; Britton, 2014). NMR spectroscopy is a flexible and powerful method for reaction monitoring or quantitative chemical analysis (Stanisavljev et al., 1998; Williamson et al., 2019). The NMR study of batteries is often associated with broad line widths inherent to solid state materials. For *in operando* investigations of liquid state electrolysis systems, high spectral resolution is a critical factor. The determination of structural information for small molecules relies on the detection of minor changes in chemical shifts and J-couplings in the range of a few Hertz. Thus, signal line widths are of major concern since the earliest publications in this area of research. Several experiment setups for the electrochemical reduction and/or oxidation of organic molecules are suggested in literature (Bussy and Boujtita, 2015; Falck and Niessen, 2015). The first *in operando* flow cell for the investigation of electrochemical processes consisted of a two-electrode setup inside a 5 mm NMR tube (Richards and Evans, 1975). A Pt/Hg wire working electrode outside the sensitive volume was placed inside a 3 mm tube concentric to the NMR tube. At the bottom of the 3 mm tube, a capillary released the reaction products into the sensitive volume of the 5 mm tube. The setup allowed sample spinning, which was required due to the low spectral resolution of the spectrometer at that time. This approach was then adapted for the investigation of anion radical decays and improved by using three electrodes (Mairanovsky et al., 1983).

An alternative *in operando* setup employed thin film electrodes to minimize distortions of the B_0 and B_1 field by conductive parts of the electrolysis cell (Mincey et al., 1990) where ^{1}H line widths of 0.9 Hz could be achieved (Prenzler et al., 2000; Webster, 2004; Zhang and Zwanziger, 2011). Additionally, radio frequency (RF) chokes were introduced to this setup to minimize interactions between NMR and the potentiostat (Webster, 2004). However, manufacturing of thin film electrodes is not easily adaptable. An alternative setup was constructed with improved accessibility (Klod et al., 2009). The electrolysis cell employed carbon fiber electrodes with a high surface area and could be set up without need for special equipment (Bussy et al., 2013). However, the use of carbon fiber electrodes limits the variety of possible electrocatalysts.

A different technique for the coupling of electrochemistry and magnetic resonance is hyphenated electrochemical NMR (Albert et al., 1987; Falck et al., 2013; Simon et al., 2012), where the electrochemical cell is physically separated from the

NMR spectrometer by passing the electrochemically generated species to an NMR probe by flow. This technique does not suffer from B_0 and B_1 distortions, but there is a time delay between generation and detection of the electrochemical species due to the physical separation.

To directly monitor paramagnetic species, electron paramagnetic resonance (EPR) spectroscopy was employed in a recent study as a screening tool for electrocatalysts (Neukermans et al., 2020).

Despite their first appearance in 1975, electrochemical *in operando* NMR investigations of liquid state systems are tested primarily on well-studied, simple redox systems. More recently *in operando* NMR has been used to study biological systems (Zhang and Zwanziger, 2011; Bussy et al., 2013; Falck et al., 2013). However, this method has not yet been utilized for the investigation of industrial and energy applications, *e.g.* the electrolytic reduction of CO_2.

The majority of research was performed using ^{1}H NMR due to the high sensitivity compared to other nuclei with only few attempts made to investigate ^{13}C systems (Albert et al., 1987). ^{13}C NMR offers a high spectral width and thus allows for an increased separation between signals, but suffers from a low natural abundance of the nucleus. To increase the sensitivity, steady-state free precession (SSFP) was suggested to achieve a high signal-to-noise ratio (SNR) during short measurement times despite using non-enriched samples (Nunes et al., 2014).

In operando ^{13}C NMR spectroscopy is ideally suited to study the electrolytic reduction of CO_2 to CO, which requires high resolution to monitor changes in the structure of the educt and the ability to use high sensitivity NMR equipment. To investigate processes of interest directly, the working electrode needs to be placed in the sensitive volume of the NMR coil. On the other hand, conductive components in the sample can lead to distortions of B_0 and B_1. These effects can be minimized by proper placement and orientation of the electrode and by pulse sequences that are robust against B_0 and B_1 field distortions (Hargreaves et al., 2011; Britton et al., 2013; Romanenko et al., 2014; Jungmann et al., 2017). For a versatile cell setup, ease of construction, adaptability for various metal electrodes and the applicability in unmodified NMR liquid state probes is desirable.

This work presents an electrolysis cell for the *in operando* NMR investigation of electrolytic CO_2 reduction. The cell is constructed inside a 5 mm NMR tube and consists of a three-electrode setup, which can easily be adapted. The electrochemical performance of the setup was evaluated by characterizing CO_2 in an 1 M $KHCO_3$ electrolyte with a) all neccessary electro-chemical equipment connected and b) without connection.. To investigate the mobility and interactions of the reactant and the electrolyte, T_1, T_2 and exchange time constants between CO_2 and HCO_3^- were determined.

2 *In operando* NMR setup

2.1 Electrolysis cell

The three-electrode electrolysis cell fits a standard 5 mm NMR tube and consists of a 2.5 x 4 x 0.05 mm silver foil (GoodFellow, Hamburg, Germany) with an area of 10 mm^2 as working electrode and a graphite rod with 1 mm diameter and 50 mm length (GoodFellow, Hamburg, Germany) as counter electrode. A chlorinated silver wire tip with a diameter of 0.25 mm (GoodFellow, Hamburg, Germany) was employed as micro Ag/AgCl reference electrode. All electrodes were connected using silver wire with a diameter 0.25 mm, insulated with polytetrafluoroethylene (PTFE) of 0.024 mm thickness (GoodFellow, Hamburg,

Germany). A graphite counter electrode prevents the dissolution of metals during electrolysis and which may deposit at the working electrode resulting in a change of catalytic properties (Benke and Gnot, 2002). This process becomes pronounced for small setups with half-cell reactions not separated by a membrane since species originating at the counter electrode diffuse sufficiently fast towards the working electrode.

To join the silver lead wire and the silver foil the wire insulation was stripped off over a length of about 1–2 mm. The skinned wire tip was pressed onto the silver foil while heating to 450 °C for a few seconds using a soldering iron. The counter electrode was connected by soldering where *ca.* 2 cm of the silver wire insulation was removed and wrapped around one end of the graphite rod.

The reference electrode was prepared by cleaning the stripped tip (*ca.* 2 mm) of a silver wire in concentrated nitric acid for 30 seconds. The electrode was subsequently transferred into an 1 M aqueous solution of potassium chloride ($\geq$ 99.5 purity; Sigma Aldrich, Munich, Germany) for 30 minutes. During this process a thin layer of silver chloride (AgCl) formed, creating a micro Ag/AgCl reference electrode (Inzelt, 2013). The averaged potential of the micro Ag/AgCl electrode was determined to be 0.132 ± 0.004 V *vs.* a commercial Ag/AgCl (3 M KCl) reference electrode in 1 M $KHCO_3(aq)$. Potentials provided in this work are given *vs.* the micro Ag/AgCl electrode. The commercial electrode was specified with a potential of 0.210 V *vs.* normal hydrogen electrode (NHE). Thus, the potential of the micro Ag/AgCl reference electrode was determined as of 0.342 ± 0.004 V *vs.* NHE in CO_2 saturated 1M $KHCO_3$. The potential of the micro reference electrode was constant during one experiment, but may vary slightly in different chemical environments.

The electrodes were arranged in a geometry as shown in Figure 1a and fixed using PTFE tape and a heat shrink tubing. The distance between the center of the working electrode and the reference electrode was adapted to the height of the sensitive volume of the NMR coil. The position of the working electrode inside the 5 mm tube was adjusted to match the center of the coil. This arrangement minimizes the content of conductive material inside the NMR coil, thus reducing distortions of B_0 and interactions with B_1. Additionally, a minimized distance between the reference and the working electrode ensures a small uncompensated resistance of $5 \pm 2 \ \Omega$ and correspondingly a small internal resistance (iR) drop for all electrochemical measurements. An iR drop is a drop in the potential for an electrochemical system caused by the uncompensated resistance according to Ohm's law. Thus, the iR drop is proportional to the uncompensated resistance and the applied current.

The lead wires of the electrodes were passed through a drilled opening of an NMR tube cap. Cellulose nitrate glue (UHU HART, UHU, Bühl, Germany) was applied to the top of the tube cap and the protruding connection wires for mechanical stability. The glue fixes the position of the electrodes inside the 5 mm tube and seals the drilled opening in the cap. Additionally, ethyl cyanacrylate glue (Loctite 406, Henkel, Düsseldorf, Germany) was applied on the top after the cellulose nitrate glue hardened in order to decrease the gas permeability.

2.2 Cell holder

The holder for the electrolysis cell is shown in Figure 2. The setup enables an easy and stable connection between the thin silver wires of the cell and the shielded coaxial cables of the potentiostat. Furthermore, it increases the structural stability
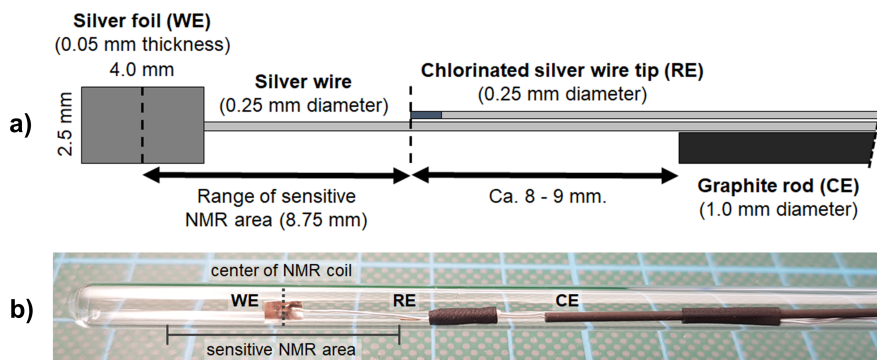
Figure 1. (a) Geometry and arrangement of the three-electrode *in operando* NMR setup. It consists of a silver foil working electrode (WE), a graphite rod counter electrode (CE) and a micro Ag/AgCl reference electrode (RE). The reference electrode was placed on the edge of the sensitive NMR area to minimize the amount of conductive material during NMR measurements while maintaining a small ohmic potential drop between working and reference electrode. (b) Photograph of the electrode setup inside a 5 mm tube.

of the cell by reducing the weight and strain as well as vibrations of the coaxial cables. The frame of the cell holder was 3D-printed using acrylnitrile butadiene styrene (ABS) copolymer (Filamentworld, Neu-Ulm, Germany). For each electrode a non-magnetic SMA coaxial connector (model 23_SMA-50-0-13/111_NE, Huber+Suhner, Herisau, Switzerland) was fixed to the frame using non-magnetic screws. To connect the electrolysis cell, the silver wires were soldered to the connector pins. The bottom hole of the cell holder was adjusted to the outer diameter of the NMR tube plus the tube cap. The 5 mm tube containing the electrolysis cell is mounted into the cell holder from the top opening and the cell is fixed by tightly squeezing the tube cap at the top end of the NMR tube into the bottom hole of the holder.

The direct insertion of the *in operando* cell into the probe was found to be mechanically unstable. To stabilize the sample inside the magnet and to achieve a mechanical separation of probe and cell, a dismounted turbine of a magnet lift was fixed on top of the probe. A spinner (Bruker, Germany) matching the opening of the turbine was then attached to the 5 mm tube of the *in operando* cell. The sample with the attached spinner was inserted into the turbine and probe by hand. The vertical position of the *in operando* cell inside the spinner was adjusted to match the sensitive NMR volume. No sample spinning was performed.

2.3 Assembly for noise depression

The *in operando* cell was connected to a potentiostat using shielded coaxial cables with SMA connectors. The top opening of the magnet was closed with a copper plate containing two RF feed-throughs for potentiostat connection (NMR Service, Erfurt, Germany). Additionally, three low pass RF filters (SLP-5+, SLP-15+, SLP-30+, Mini Circuits, New York, USA) were connected to each cable for noise depression (Figure 3). The SLP-5+ low pass filter (<5 MHz) was connected to the copper plate connection at the top of the magnet and the SLP-15+ (<15 MHz) & SLP-30+ (<30 MHz) filters were attached to the potentiostat connections. Since the connection for the potentiostat are unshielded, a silver cloth was wrapped around all un-

Figure 2. Cell holder consisting of the 3D-printed frame (black) and three SMA coaxial connectors (white and gold). The electrolysis cell is fixed inside the cell holder and the electrode wires are soldered to the pins of the SMA coaxial connectors.

shielded cables. In addition, the body of the probe, the NMR magnet and the potentiostat were connected to a common ground. The shielding setup is shown in Figure 3.

145
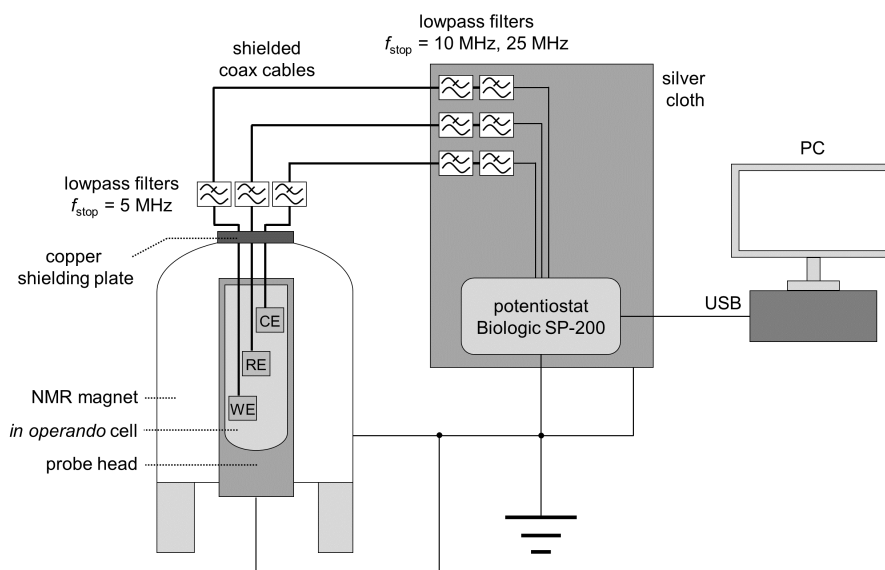
Figure 3. Schematic drawing of the *in operando* NMR electrolysis setup with shielding, RF filters and potentiostat.

2.4 Simulation of the B_1 field and the nutation behavior within the *in operando* cell

The distortion of the B_1 field in the proximity of the metal electrode was numerically simulated using EMpro (Version 2020, Keysight Technologies). A square Helmholtz coil consisting of two parallel square shaped wires with a distance of 0.5445

times the length for each side of the square, was designed to mimic a homogeneous RF field in the vicinity of the electrode.
An ideal conductor served as coil material and both squares of the coil were driven synchronously by a current source. The silver electrode was placed in the center of the coil as shown in Figure 4d. The simulation was performed for three different angles ($0°$, $45°$, $90°$) between the B_1 field and the electrode plane and data points were acquired with a resolution of 0.4 mm. The complex magnetic field vectors of the simulated volume were exported by means of a Python script (Python 3.7, Python Software Foundation) for data processing.

Eddy currents caused by the oscillating B_1 field are formed at the metal surface (Figure 4). In turn, the eddy currents induce a magnetic field that distorts amplitude and phase of the excitation pulse. The distortion of the B_1 field strongly depends on the angle between the electrode and the RF field (Britton, 2014; Romanenko et al., 2014). For a parallel configuration, *i.e.* at an angle of $0°$, distortions of the B_1 field are minimized (Figure 4a). Correspondingly, there is only a small eddy current formation due to the minimal surface area remaining perpendicular to the B_1 field.

For a perpendicular ($90°$) orientation of the electrode (Figure 4c) the B_1 field showed major distortions, which lead to a decrease in amplitude of the B_1 field in the proximity of the electrode surface. However, the B_1 field strength is increased at the top and bottom edges of the electrode. At the side edges, the direction of the field, *i.e.* the phase of B_1, changed. At a distance of about 0.8 mm from the electrode surface, the strength of the RF distortions decreased to 1/e of the B_1 field.

Smaller distortions of B_1 were observed for the $45°$ orientation of the electrode (Figure 4b), affecting mostly the direction of the field whereas the signal amplitude decreased at the surface. Major distortions of the B_1 phase were present along the top and bottom edges of the electrode. The distortions decreased to 1/e of the B_1 field strength at a distance of *ca.* 0.6 mm from the electrode surface.

It can therefore be concluded that an electrode orientation planar to B_1 is considered optimal. Amplitude and phase of the B_1 field distortions depend on the spatial orientation. However, distortions are significant in the immediate proximity of the electrode (0.6–0.8 mm from the surface). Therefore, the majority of the volume inside a 5 mm NMR tube can be regarded free of distortions for the chosen electrode geometry and thus can be probed by NMR spectroscopy without additional measures. For the current setup a minute adjustment of the orientation is not necessary. It should be noted that the distortions of the B_1 field are depending on orientation and on electrode size and adjustments can be required for larger *in operando* electrolysis cells.

Two experiments were performed to validate the B_1 field simulations and study the effect of B_1 field distortions on NMR measurements. First, a nutation experiment using distilled water was performed using a Bruker Avance III HD spectrometer with a 9.4 T wide bore magnet (400 MHz ^{1}H RF frequency) and a broadband gradient probe (Bruker DiffBB). The experiment was conducted with and without the electrode setup where the electrode orientation was either parallel, perpendicular, or in a $45°$ angle with respect to B_1. Data points were acquired at a constant pulse power of 13.9 W for pulse lengths between 5 μs and 400 μs using 5 μs steps. Nutation curves were acquired using the ^{1}H water peak due to the higher S/N ratio compared to the ^{13}C resonances of HCO_3^- and CO_2 (Figure 5a). Figure 5b shows the Fourier transform of the nutation curves. Secondly, the effect of the B_1 distortions on the water signal shape was studied. In Figure 5c the NMR signal shapes of water for different electrode
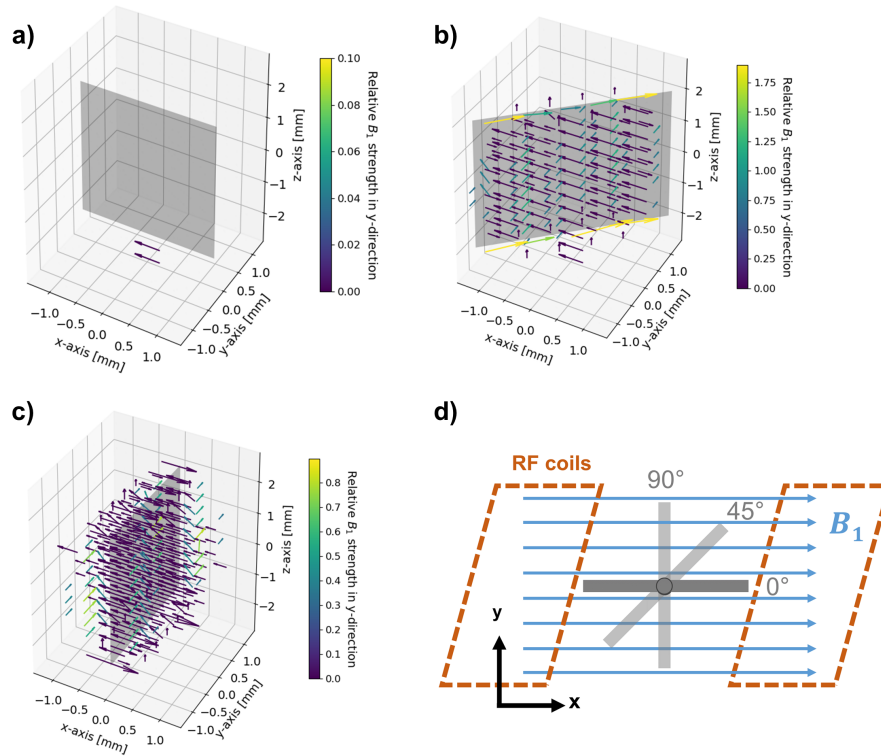
Figure 4. B_1 field simulation in proximity of the metal electrode for angles of 0° (a), 45° (b) and 90° (c) between the direction of the incoming RF field and the electrode surface, and geometry and arrangement of the metal electrode in relation to the B_1 field in the simulations (d). The incoming RF field points towards the positive x-axis. The vectors represent the deviations in field strength and direction compared to the undistorted RF field. Deviations smaller than B_1/e are not shown in order to increase clarity. For a better visibility of phase deviations, the vectors are color coded according to their relative field strength in y-direction compared to the incoming field amplitude. Note that all figures have individual colorbar ranges. No distortion is present for a parallel (0°) orientation of RF field and electrode. The angled (45°) and perpendicular (90°) orientations cause major distortions in immediate proximity to the electrode, which diminish at a distance of 0.6–0.8 mm.

orientations are compared. The B_0 field was shimmed on a sample containing pure distilled water without the electrode setup, and not reshimmed after insertion of the electrodes in order to exhibit the distortion of the B_0 field by the metal components.

As predicted by the simulations, deviations in the nutation curves are largest for the perpendicular electrode orientation and minimal for the parallel orientation compared to the neat nutation behaviour. The magnitude of deviations for the 45° electrode orientation is in between the parallel and perpendicular orientation. The nutation curve for the perpendicular orientation exhibits both, the fastest decay and the broadest distribution of nutation frequencies. This becomes evident in Figure 5b, where the perpendicular orientations feature a broad main component distributed around 25.6 kHz with an additional component at low frequencies.

All three electrode orientations exhibit minor deviations of the 90° and 180° pulse lengths compared to the pure water sample. Therefore, common pulse sequences can be applied for studies using the *in operando* cell. This is evident in Figure 5c, where only small differences due to B_0 field distortions between the unshimmed water signals for different electrode orientations are

195   apparent.
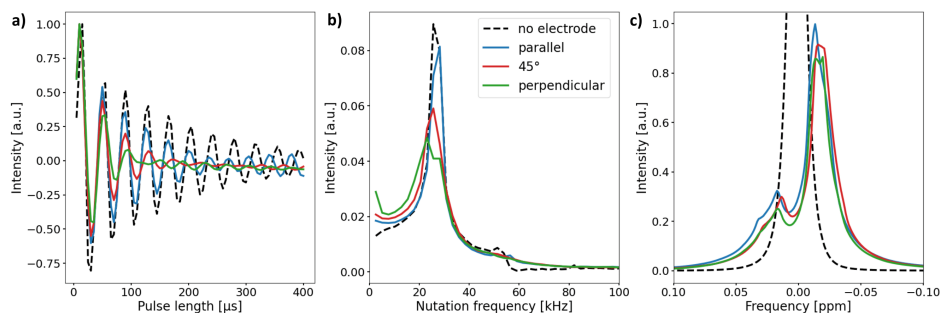
Figure 5. (a) Nutation curves of the ^{1}H water resonance using the the *in operando* cell with electrode orientations of 0° (blue), 45° (red) and 90° (green). The nutation curve of a water sample without electrode is shown for comparison (black dashed line). Deviations from the undistorted nutation curve is largest for the perpendicular electrode orientation, and minimal for the parallel orientation. (b) Fourier transform of the nutation curves. The main component of the undistorted sample nutates at a frequency of 25.6 kHz (15 μs 90° pulse length). For the samples with electrode setup, the width of the main component increases and a low frequency component appears. (c) ^{1}H water NMR spectrum with and without electrode setup. The B_0 field was not shimmed after electrode insertion. The signal shape is mainly governed by B_0 field distortions and only slightly affected by deviations in the B_1 field.

All simulations and NMR measurements on the orientation dependent magnetic field distortions caused by metallic components are in line with literature (Ilott et al., 2014; Serša and Mikac, 2018). In these studies an electrode orientation parallel to the B_1 field direction is considered optimal. Strong B_1 field distortions as well as signal loss in the proximity of the metal are observed for perpendicular orientations. It was also shown that angled orientations lead to amplification of the B_1 field along

200   the metal boundaries, which is consistent with the pronounced distortions of B_1 field strength and phase alterations observed for the 45° electrode orientation.

3   Materials and methods

A 1 M aqueous solution of 98% [13]C enriched $KHCO_3$ (Sigma Aldrich, Munich, Germany) was used as electrolyte. The electrolyte was pre-chilled inside a polyethylene vial in a 10 °C water bath. *Ca.* 1 mL of chilled electrolyte was filled into a

205   5 mm NMR tube and saturated with 99% [13]C enriched CO_2 (Cambridge Isotope Laboratories, Tewksbury, USA) by bubbling for 20 minutes at a temperature of 10 °C if not stated otherwise. The CO_2 was bubbled into the electrolyte using a 1/16 inch PEEK tube, and the flow rate was adjusted to *ca.* 0.3 mL/s. The three electrode setup was placed inside the 5 mm tube filled with CO_2 saturated electrolyte, ensuring that the contact between counter electrode and silver wire was not immersed in liquid.

Prior to sealing, the gas phase inside the tube was aerated with ^{13}C labeled CO_2 gas. All preparation steps were performed under ambient conditions.

The electrochemical experiments were performed using a BioLogic SP-200 potentiostat (BioLogic Science Instruments, Seyssinet-Pariset, France) at a temperature of 10 °C, controlled by a surrounding water bath. The electrochemical performance of the *in operando* cell was evaluated using chronopotentiometry (CP) at several current densities up to 4 mA/cm^2 for 15 minutes each and linear sweep voltammetry (LSV) in the range of -1.0 V to -2.5 V *vs.* Ag/AgCl (rate 10 mV/s) afterwards. Between the electrochemical experiments the system was allowed to relax for 5 minutes. An equivalent chronopotentiometry experiment was performed using a 1 cm^2 silver electrode and reference and counter electrodes of identical size and material. This experiment serves as reference. The reference chronopotentiometry experiment was performed in a cleaned glass beaker filled with 60 mL of aqueous CO_2 saturated 1 M $KHCO_3$ electrolyte, denoted as bulk cell. Working and counter electrode were arranged in a parallel geometry inside the bulk cell. All distances between working and counter electrode and between working and reference electrode are identical to the *in operando* cell.

The potential of the micro reference was determined *vs.* a commercial Ag/AgCl reference electrode with a double junction system and a 3 M aqueous KCl bridge electrolyte. The measurement was performed using the electrolyte of the CO_2 electrolysis where the reference electrode potential was averaged over 10 minutes. Both reference electrodes were equilibrated for 10 minutes prior to the experiment.

All ^{13}C NMR measurements were performed using a Bruker Avance III HD spectrometer with a 14.1 T widebore magnet (150.9 MHz RF frequency for ^{13}C) and a broadband gradient probe (Bruker DiffBB). 90° pulses were achieved using a pulse length of 15.5 μs and a pulse power of 58.7 W, and the relaxation delay was set to 85 s. Spectra were post-processed by applying a 1 Hz line broadening. NMR experiments were performed at a temperature of 10 °C if not stated otherwise. Concentrations of the carbon species in the CO_2 saturated electrolyte with CO_2 atmosphere were determined using a sealed NMR tube using sodium trimethylsilylpropanesulfonate (DSS) (Sigma Aldrich, Munich, Germany) as reference (c(DSS) = 61.62 mM) and a ^{1}H WALTZ-16 sequence for decoupling (Shaka et al., 1983; Tenailleau and Akoka, 2007). The chemical shift scale of all ^{13}C spectra was referenced to the frequency offset of DSS. DSS was not employed for *in operando* experiments because the organic salt can alter the electrochemical behavior. The CO_2 saturated electrolyte was examined using longitudinal, T_1 and transverse, T_2, relaxation and exchange time measurements. T_1 relaxation time constants were determined using a saturation recovery pulse sequence with equispaced saturation pulses using logarithmically spaced recovery times between 1 s and 128 s. Transverse relaxation time constants were determined using a Carr–Purcell–Meiboom–Gill (CPMG) pulse sequence with an echo time of 5 ms (Carr and Purcell, 1954; Meiboom and Gill, 1958). The exchange time between HCO_3^- and solvated CO_2 was assessed by a 1D exchange spectroscopy (EXSY) sequence (Bain and Cramer, 1993), which uses a shaped Gauss pulse with 100 Hz bandwidth for the selective inversion of the bicarbonate resonance at 160.7 ppm. The center frequency of the selective inversion pulse was adjusted in case of a HCO_3^- frequency shift.

The exchange time constant T_{exc} was determined by fitting the evolution of the CO_2 signal integral $I(CO_2)$ as a function of the mixing time τ_m to

$$I(CO_2) = I_0(CO_2) \left\{ 1 - 2 \left[\exp\left(-\frac{\tau_m}{T_{exc} + T_1}\right) - \exp\left(-\frac{\tau_m}{T_1}\right) \right] \right\}, \tag{1}$$

where I_0 is the signal integral at $\tau_m = 0$. This simplified fitting equation is valid under the conditions that the bicarbonate
245   concentration substantially exceeds the CO_2 concentration and both species possess identical T_1 times (Bain and Cramer, 1993).

4   Results and discussion

4.1   Electrochemical performance of the *in operando* electrolysis cell

The time dependent potential curves for the chronopotentiometry measurements are shown in Figure 6a. The potentials ob-
250   served for both the *in operando* and the bulk cell are within the range reported in literature, as the values depend on the properties of the catalyst and the electrolysis cell. CO_2 electrolysis starts at -1.33 V *vs.* Ag/AgCl for the *in operando* cell and at -1.23 V *vs.* Ag/AgCl for the bulk cell. However, three types of deviations could be deduced from the potential curves for the *in operando* cell compared to the bulk cell. First, higher overpotentials are observed. Second, it took longer for the *in operando* cell t to equilibrate when the current is applied and switched off. Third, increasing oscillations in the potential and additional
255   noise are observed, starting at -1 mA/cm^2.

The non-parallel geometry of the electrodes in the *in operando* cell may be causing the first two deviations. For a parallel geometry the distance between the working electrode and the counter electrode is approximately constant across the whole WE surface. Thus, the iR drop is constant across the electrode and the surface potential is uniform. However, in a non-parallel geometry, there is a spatially dependent iR drop between working and counter electrode, which leads to non-uniform potential
260   distribution across the electrode surface. As a result, electrolysis preferably takes place at the closest region between working and counter electrode, where the iR drop is minimal. The CO_2 concentration within that region decreases during electrolysis and thus the concentration overpotential increases. When the concentration overpotential exceeds the increase in iR drop for a more distant region the electrolytic process shifts to that location.

For the electrode setup used in the *in operando* cell, the edge of the silver sheet is the region of the working electrode
265   closest to the counter electrode. For a current density of -0.25 mA/cm^2, the electrolytic CO_2 reduction at the silver foil edge takes place at an identical overpotential compared to the bulk cell . However, because of the small area the electrolysis at the electrode edge is not sustainable and therefore the diffusive CO_2 transport becomes limited. As a result, the CO_2 concentration is depleted after 2 minutes of electrolysis. At this point, CO_2 reduction takes place at the next-nearest region of the counter electrode, a portion of the silver foil plane, where CO_2 is more readily regenerated by diffusion. However, the iR drop at the
270   silver foil plane is increased compared to the edge and thus the potential decreases.

With increasing current density, CO_2 conversion increases. Therefore an increasing area of the silver electrode surface with an increasing distance to the counter is used for reduction. This results in a rising iR drop and a further increasing overpotential
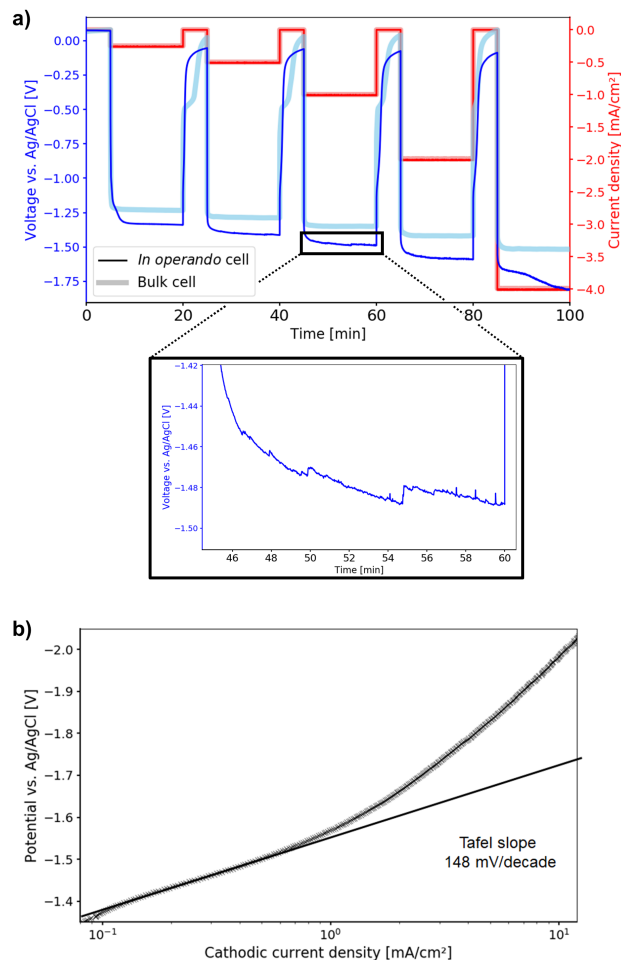
Figure 6. (a) Time depended potential curves during the chronopotentiometry measurement. Electrolytic reduction of CO_2 starts at -1.33 V *vs.* Ag/AgCl for the *in operando* cell. Compared to the bulk cell, higher overpotentials are observed. Starting at 1 mA/cm^2, oscillations and increased noise appear, which are caused by stuck product gas bubbles. (b) Tafel plot of the electrolytic CO_2 reduction in the *in operando* electrolysis cell. The Tafel slope was determined in the low current density region as 148 mV per decade, resulting in a transfer coefficient of 0.38 at 10 °C.

compared to the bulk cell. This effect may also cause the instability in potential of the *in operando* cell at a current density of -4 mA/cm^2. It is important to separate this effect from the expected increase in concentration overpotential with increasing current density, which was also observed for the bulk cell.

The oscillations and increased noise observed for the potential curve of the *in operando* cell at higher current densities are caused by the formation of gaseous products, *i.e.* CO and H$_2$, in the confined cell geometry. The gas bubbles tend to stick to the glass walls, the electrodes or the connection wires, until they reach a sufficient size to detach and rise to the top. Diameters up to 1/3 of the size of the electrode surface were observed for the gas bubbles. These bubbles blocked significant fractions of the electrodes, thus affecting the electrochemical measurements. For the bulk cell, only a small percentage of gas bubbles adsorbed on the electrodes or the cell did not stuck due to the larger distance between the electrodes and the glass walls. Moreover, the larger electrode was affected by the comparatively smaller gas bubbles.

For the *in operando* cell, the Tafel slope was determined as 148 mV per decade from current–voltage (IV) curves of the LSV experiments in the low current density region as shown in Figure 6b. In this region no mass transport limitations for the electrolytic reduction of CO$_2$ occurred. The slope of the Tafel plot translates to a charge transfer coefficient of $\alpha = 0.38$. From literature, values for the Tafel slope can range from 130 mV to 140 mV per decade, resulting in charge transfer coefficients of 0.41 – 0.45 for comparable systems at room temperature (Hori et al., 1987; Hatsukade et al., 2014; Lu et al., 2014; Hsieh et al., 2015). The minor discrepancy between measured and literature values may originate from the lower temperature where experiments were performed, what results in a lower thermal energy for the activation of processes and thus lower diffusion rates.

Overall, the *in operando* cell shows a comparable performance to a bulk electrolysis cell in the low current density range, *i.e.* below -1 mA/cm^2. Due to the non-parallel cell geometry there is a spatially dependent iR drop distribution across the working electrode surface, which is unfavorable for electrolysis experiments. Since this effect is more pronounced for larger electrode geometries it is crucial to reduce the working electrode size. However, a larger electrode area is beneficial for minimizing the current density during electrolysis and thus the concentration overpotential. The 10 mm^2 electrode used in the *in operando* cell represents a compromise between both considerations. Nonetheless, the potential becomes unstable at higher current densities and electrochemical measurements may be distorted by gas bubbles stuck in the confined glass tube.

4.2 NMR evaluation of the *in operando* electrolysis setup

The ^{13}C spectrum of CO$_2$ saturated electrolyte is shown in Figure 7a. Both signals in the spectra are assigned to HCO$_3^-$ at 160.7 ppm and solvated CO$_2$ at 124.7 ppm (Abbott et al., 1982; Liger-Belair et al., 2003; Mani et al., 2006). The low solubility of carbon dioxide in water causes a weaker signal compared to bicarbonate. No signal of gaseous carbon dioxide could be observed since the gas phase inside the NMR tube is outside of the sensitive volume of the RF coil. For a measured pH of 8.2 ± 0.15 after CO$_2$ aeration of the electrolyte, about one percent of dissolved carbonate is expected. However, due to the fast exchange of HCO$_3^-$ and CO$_3^{2-}$, signals for both species coalesced into one peak.

The concentrations of the carbon species in the CO$_2$ saturated electrolyte are shown in Table 1. During aeration of the electrolyte with CO$_2$ the concentration of bicarbonate (HCO$_3^-$) increased by a factor of two. The measured concentration of
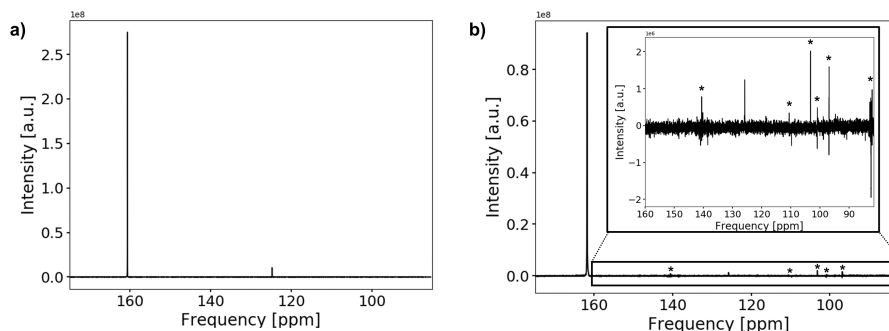
Figure 7. ^{13}C spectrum of the CO_2 saturated electrolyte without (a) and with (b) electrodes. Measurements with electrodes include connection cables and a powered potentiostat, but no shielding. The peak positions of bicarbonate and solvated carbon dioxide are at 160.7 ppm and 124.7 ppm, respectively. Peak positions are shifted downfield by about 1.1 ppm when the conductive components are introduced. The spectrum in b) suffers from increased noise as well as from external RF signals, which are comparable in intensity to the CO_2 signal. External RF signals have been marked with (*).

CO_2 is in the uncertainty limits of the theoretical equilibrium concentration for aqueous solution ($c_{1013\,hPa,\,10\,°C}$ = 52.7 mM) (Sander, 2015). The uncertainty is caused by a combination of a weak signal-to-noise ratio of the DSS methyl group reference signal and imperfections of the temperature control ($\leq$ 1°C).

Table 1. Concentrations of carbon species in CO_2 saturated electrolyte at 10 °C and 1013 hPa CO_2 pressure.

Carbon species	Concentration [M]
HCO_3^-	1.82 ± 0.14
CO_2	$(55.0 \pm 4.4) \cdot 10^{-3}$
Total carbon	1.87 ± 0.14

310   As the solubility of CO_2 in water is low, the ^{13}C signal of CO_2 is weak even for using ^{13}C labeled and fully saturated samples. It is therefore essential to optimize the signal-to-noise ratio before experiments. To investigate the effect of the *in operando* setup on the ^{13}C spectra, the signal-to-noise ratio of the HCO_3^- signal was determined under different conditions (Table 2). Decreasing the temperature from 22 °C to 10 °C significantly improved the signal-to-noise ratio. As CO_2 shows a higher solubility at lower temperatures (*cf.* $c_{1013\,hPa,\,22\,°C}$ = 38.0 mM) (Sander, 2015), the signal-to-noise ratio of the CO_2

315   signal increased by a factor of *ca.* 1.4. The equilibrium constant for the CO_2/HCO_3^- equilibrium changed by only 1% due to the decrease in temperature. Therefore an increase in CO_2 concentration causes a similar increases of HCO_3^- in solution. The decrease of 12 °C also increases the equilibrium magnetization and reduces thermal noise which led to an increase in the signal-to-noise ratio of about 6%.

Table 2. signal-to-noise ratio of the ^{13}C HCO$_3^-$ signal under different conditions.

Temperature [°C]	Conditions	signal-to-noise ratio [-]
	No conductive material	1247
22	*In operando* cell	397
	In operando cell and connection cables	290
	No conductive material	1994
10	*In operando* cell and connection cables	399
	Full *in operando* electrolysis setup with shielding	2510

After introducing the electrodes into the magnet the signal positions shifted downfield by 1.1 ppm and line widths became significantly broader but could be reduced to about 1 Hz by shimming except for a downfield shoulder. The signal-to-noise ratio of the spectrum was reduced significantly by 68%. As the concentration of the carbon species remained unchanged, the decrease in the signal-to-noise is a combined effect of increased noise levels and a reduced quality factor, Q, of the NMR circuit caused by the conductive components. As shown in Figure 7b, the main contribution is the introduction of external RF noise due to the metallic components and cables acting as radio antenna. Coherent external RF noise in the frequency range of ^{13}C NMR at 14.1 T (150.9 MHz) is caused by mobile radio communication (Bundesnetzagentur, 2019). Introducing additional connections to the setup as well as connecting the cell directly to a powered potentiostat further decreased the signal-to-noise ratio despite using shielded coaxial cables. A highly shielded setup as described in Figure 3 is therefore necessary to decrease RF noise originating from external sources in order to obtain signal-to-noise ratios comparable to experiments without conductive materials. Using just single elements of the shielding setup, *i.e.* only the copper plate for the top opening of the magnet, the silver cloth, the common ground, or the filters, does not restore the signal-to-noise ratio to original values.

As a reference for the CO_2 saturated electrolyte, longitudinal relaxation times and exchange rates were determined using a standard NMR tube without the electrolysis setup. In a second step the electrodes and leads were introduced but not connected. In the final step data were collected with the full electrolysis setup shown in Figure 3. All results are summarized in Table 3. The larger errors of the CO_2 rates are caused by a low signal-to-noise ratio of the carbon dioxide signal.

First, the changes in relaxation and exchange behavior after insertion of the electrodes are discussed. The longitudinal relaxation times for HCO$_3^-$ and CO_2 remain unchanged within error boundaries compared to the electrolyte without conductive material. However, the exchange time constant of the chemical equilibrium between CO_2 and HCO$_3^-$ decreased from 5.23 s to 3.31 s. The T_2 time constant for both HCO$_3^-$ and CO_2 decreased after the introduction of the electrolysis cell. The faster chemical exchange between both carbon species can only be a minor contribution to the decreased T_2 values, in particular for HCO$_3^-$, as it is present in significantly higher concentrations than CO_2. Additional contributions could be caused by local motion in the vicinity of the electrode, which may exceed the mobility due to self-diffusion by several orders of magnitude higher

Table 3. Relaxation and exchange times for bicarbonate and carbon dioxide without conductive materials, with the disconnected electrolysis cell, and with full electrolysis setup at 10 °C. The full electrolysis setup included the *in operando* cell, connection cables, a powered potentiostat and shielding equipment. For measurements using the electrolysis setup no electrochemical experiments were conducted.

		Without conductive materials	With electrolysis cell	With full electrolysis setup
HCO_3^-	T_1 [s]	18.59 ± 0.08	18.56 ± 0.05	12.25 ± 0.02
	T_2 [s]	2.04 ± 0.00	1.40 ± 0.00	0.97 ± 0.00
CO_2	T_1 [s]	20.15 ± 0.59	19.55 ± 0.42	13.99 ± 0.65
	T_2 [s]	4.15 ± 0.11	2.03 ± 0.05	2.66 ± 0.21
	T_{exc} [s]	5.23 ± 0.18	3.31 ± 0.25	3.79 ± 0.37

(Benders et al., 2020). In the disconnected electrolysis cell setup, such an increased mixing could originate from concentration gradients of the electrolyte near the electrode surface due to double layer formation, possibly supported by convective flow from local heating of the electrolyte near the electrode surface. Eddy currents induced in the silver metal by the RF field of the
345 NMR pulse excitation could cause such a local heating.

The change in the exchange time is assumed to be an indirect effect of the interaction of HCO_3^- with the polarizable silver metal electrode surface. The positively charged metal surface, as observed in the absence of an external potential (Figure 6a), acts as a catalytic center for the CO_2/HCO_3^- equilibrium reaction by stabilization of intermediate compounds and thus decreasing the exchange time. Catalytic acceleration of the CO_2/HCO_3^- equilibrium is well known for biological systems in the
350 form of the carbonic anhydrase enzymes, which stabilize the negatively charged oxygen atoms by metal cations in a similar way during the CO_2/HCO_3^- exchange reaction and increases the reaction rate by six to seven orders of magnitude (Lindskog, 1997; Grisham and Garrett, 2010). The interaction of ions with metal surfaces by induction of dipoles is reported in literature to extend up to 1 nm from the metal (Seitz-Beywl et al., 1992; Bonzel, 1988; Mendonca et al., 2012), which can regarded insignificant to cause the observed changes. However, in combination with an increased mixing between surface and bulk species
355 within the sample tube, as presumed from the T_2 alterations, such an effect could be amplified.

Secondly, changes after connection of the full electrolysis setup are examined. During the measurements employing the full *in operando* electrolysis setup, the cell was connected to the potentiostat. The potentiostat was powered on, but no electrochemical experiment was conducted. Therefore the cell operates in a open circuit voltage (OCV) mode with no current flow between
360 electrodes but the voltage continuously measured by the potentiostat. Compared to the experiments with the disconnected electrolysis cell, a variation of the exchange time constant between carbon dioxide and bicarbonate cannot be precluded but is within error. However, the longitudinal ^{13}C relaxation time constant for bicarbonate and CO_2 and the transverse relaxation

time constant for bicarbonate were found to be smaller. As the experimental setup inside the sensitive volume of the NMR coil remained unchanged, the leads and filters as well as the potentiostat may be the driving forces for the increased relaxation rates. Even the continuous voltage measurements by the powered potentiostat cause a minuscule current flow between the cell and the potentiostat, this should not have a considerable influence on the double layer formation and the mobility of the electroactive species, since the potentiostat input is terminated with high impedance. Furthermore, it is improbable that increased stochastic fluctuations of magnetic fields originating from the potentiostat are causing such an increase in the relaxation rates. While powering the potentiostat induces increased RF noise in the NMR experiment, these fluctuations are successfully removed by the filters described in subsection 2.3.

A more probable source for the altered relaxation behavior is the changed capacity of the electrode assembly. Cables and filters can contain or act as capacitors and can provide additional mass, which changes the capability of the setup to dissipate or provide electrons at the electrodes. As OCV is an electrostatic mode of operation, the assembly may act as an additional supply or sink of electrons and thus affect double layer formation. This in turn may affect the whole electrolyte, *e.g.* by changing the equilibrium between the ionic species which may alter the pH of the system. This is known to sensitively affect relaxation properties for aqueous carbonate solutions (Moret et al., 2013). While a detailed analysis of these processes is outside the scope of the study it highlights the sensitivity of ^{13}C NMR to investigate fundamental processes occurring during CO_2 electrolysis, thereby justifying the efforts necessary to achieve sufficient sensitivity and resolution for *in operando* experiments. It also demonstrates the importance for a properly designed electrolysis setup and measurement protocol to avoid unwanted side effects.

The results also show that the measurement setup may affect an electrochemical system. It can influence the state of the electrodes and thus their interactions with the CO_2 saturated electrolyte. The NMR measurements with disconnected and connected electrolysis setup show that necessary equipment for electrochemical testing may affect the equilibrium state of the electrolysis. This is particularly pronounced at very low current densities or at OCV.

4.3 *In operando* NMR of the OCV evolution

The ^{13}C NMR spectra of the aqueous HCO_3^-/CO_2 sample during OCV and the potential between working and reference electrode are shown as a function of time in Figure 8. The current density between working and counter electrode remains fixed at 0 mA/cm^2 during measurements. Therefore, no gaseous products were formed during this study. During the first 5 hours of the experiment the potential drops from -31 mV to -42 mV *vs.* Ag/AgCl. After 12 hours the potential plateaued at -45 mV *vs.* Ag/AgCl and approaches equilibrium of -47 mV *vs.* Ag/AgCl after 17 hours.

The ^{13}C NMR resonances of HCO_3^- and CO_2 remained at the initial position compared to the reference measurements. A narrow main resonance with a broader shoulder persisted throughout the OCV stage. Fitting both signals with to a Lorentzian line shape, a peak separation of 0.04 ppm (6.1 Hz at 14.1 T) is obtained. The shoulder is assumed to be caused by B_0 field distortions in the proximity of the working electrode, which cannot be corrected by shimming.

The HCO_3^- signal shifted downfield about 0.007 ppm during the first 5 hours (Figure 8a), whereas the CO_2 signal shifted by 0.002 ppm (Figure 8b). Therefore, the evolution of the two signal positions appears not only to be caused by extrinsic factors
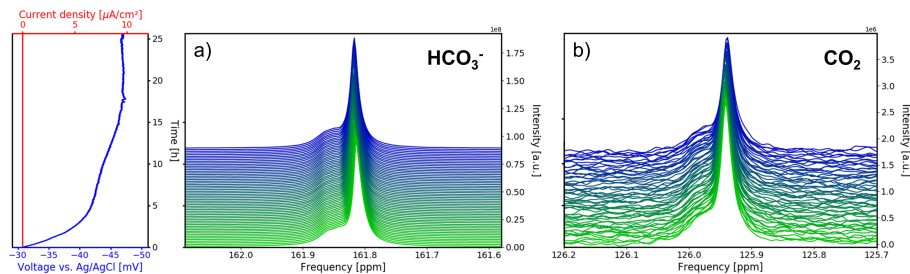
Figure 8. Time evolution of the ^{13}C signals for HCO_3^- (a) and CO_2 (b) during the OCV stage versus electrochemical potential between working and reference electrode and current density between working and counter electrode. In each sub panel the time dependent potential and current density is shown on the left with the corresponding spectra are given on the right. After a relaxation period the potential remains at a stable at 47 mV.

such as a magnet drift. After 12 hours, he HCO_3^- signal integral has increased by *ca.* 1% compared to the initial intensity (Fig-
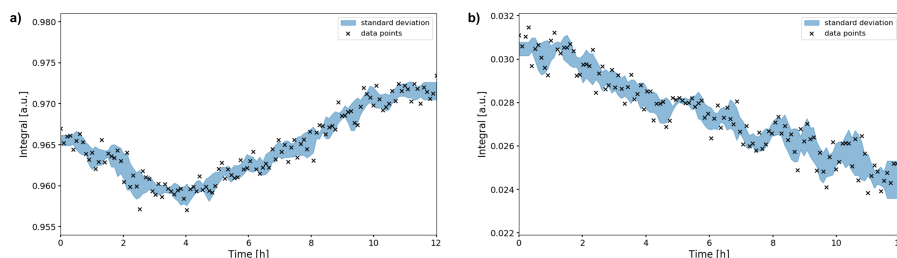
Figure 9. Time evolution of the HCO_3^- (a) and CO_2 (b) signal integrals during the OCV stage. The integrals were normalized to their maximum values during the *in operando* experiment. Error boundaries are shown in blue. The HCO_3^- signal fluctuates within the 1% range, while the CO_2 signal decreases significantly in intensity over the 12 hour period, down to 78% of its maximum value.

ure 9a). The evolution of the HCO_3^- signal position and the intensity imply an evolution of the $CO_2/HCO_3^-/CO_3^{2-}$ equilibrium since a higher chemical shift is associated with an increase of the CO_3^{2-} concentration (Abbott et al., 1982).

400   The intensity of the CO_2 peak continuously decreases during the OCV stage. After 12 hours the CO_2 signal integral decreased to 78% of the initial value (Figure 9b). Using 55.0 mM as initial concentration, as was determined in the reference experiment, this equals a concentration of 42.9 mM. After 25.6 hours of OCV, the CO_2 signal intensity decreased to 62% (34.1 mM). This is unexpected as no CO_2 has been converted by electrolytic processes during the OCV stage.

Leakage of CO_2 gas during the NMR experiment is unlikely in these amounts. Permeation of carbon dioxide through the
405   polypropylene tube cap or the glue used for sealing can be excluded, as the CO_2 gas permeability for these materials is low (Hasbullah et al., 2000). Furthermore, any CO_2 loss should be compensated by the CO_2/HCO_3^- equilibrium reaction, thus decreasing the HCO_3^- concentration. However, no sustained decrease in HCO_3^- concentration was observed. Furthermore, the total amount of all carbon species is unchanged after 12 hours of OCV. Therefore, no CO_2 was lost from the setup.

These observations indicate that the CO_2 saturated electrolyte is not at equilibrium in the initial state of the experiment. Directly after preparation, the pH value of the electrolyte was 8.2 ± 0.15. Given a total concentration of 1.87 M for all carbon species, the equilibrium concentration of solvated CO_2 at that pH value is 33.7 mM. Therefore, the initial CO_2 concentration of 55.0 mM is above the equilibrium value. The CO_2/HCO_3^- system approaches equilibrium at the end of the OCV experiment where the CO_2 concentration equals 34.1 mM.

All changes in the HCO_3^- and CO_2 signal integrals and the HCO_3^- signal position occur in accordance with the variations of the potential during OCV. Changes in HCO_3^- and CO_2 signal are associated with a shift in the electrochemical potential during the OCV stage caused by an evolution of the $CO_2/HCO_3^-/CO_3^{2-}$ concentrations towards equilibrium.

The relaxation and exchange time constants of CO_2 and HCO_3^- during the OCV stage are given in Table 4. Compared

Table 4. Relaxation and exchange time constants for bicarbonate and carbon dioxide during OCV. Experiments were conducted after the initial 12 hour OCV period.

	T_1 [s]	T_2 [s]	T_{exc} [s]
HCO_3^-	11.80 ± 0.03	0.78 ± 0.01	2.65 ± 0.28
CO_2	13.18 ± 0.71	2.15 ± 0.25	

to the reference measurement of the *in operando* cell, the exchange time decreased after the system approached equilibrium. The decrease in the exchange time is linearly proportional to the decrease in CO_2 concentration. The decreased exchange time between CO_2 and HCO_3^- affects the transverse relaxation process and decreases T_2 time constants, as discussed for the reference measurements. T_1 decreased only slightly as a result of the change in equilibrium and are overall comparable to the test of the *in operando* setup. Slight decreases in relaxation times may be the result of small variations in the electrolysis setup assembly (see reference measurements).

5 Conclusions

This study presented a setup for the in *in operando* NMR study of the electrochemical CO_2 reduction, specifically designed to observe changes in molecular dynamics in the proximity to the working electrode. It was shown that ^{13}C relaxation, exchange rates and chemical shifts can be used to sensitively characterize an electrochemical system. A key feature of the setup is the suppression of noise and external radio frequency signals introduced by conductive materials, enabling the observation of low concentration species. Relaxation and exchange experiments provide a sensitive probe for the interaction of ionic species with metal electrodes under different electrochemical conditions. The results indicated that the electrochemical measurement equipment itself may affect the reaction and molecular dynamics. A quantitative interpretation of the data requires carefully step-by-step reference measurements and a distinction between intrinsic effects caused by the investigated electro-

chemical system and extrinsic effects induced by the electrolysis setup. *in operando* NMR was employed to monitor an aqueous CO_2/HCO_3^- system for electrolytic CO_2 reduction at open circuit voltage, revealing that an (electro-)chemical equilibrium in solution evolves for considerable time after sample preparation.

Author contributions. Each author contributed to this work as follows. S. Jovanovic developed the *in operando* cell and setup with assistance of P. Schleker, P. Jakes and J. Granwehr. NMR experiments were performed by S. Jovanovic. B_1 field simulations were performed by M. Streun. Orientation dependent nutation experiments were performed by Michael Schatz. Data analysis and interpretation were performed by S. Jovanovic in collaboration with P.Schleker, P. Jakes, S. Merz, J. Granwehr and R.-A. Eichel. The manuscript was written in collaboration by S. Jovanovic, S. Merz, J. Granwehr and R.-A. Eichel. All authors have read and agreed to the manuscript.

Competing interests. The authors declare no conflicts of interest.

Acknowledgements. The author gratefully acknowledges funding by the German Federal Ministry of Education and Research (BMBF) within the Kopernikus Project P2X: Flexible use of renewable resources – research, validation and implementation of 'Power-to-X' concepts, and by the Deutsche Forschungsgemeinschaft (DFG, German Research Foundation) under Germany´s Excellence Strategy – Cluster of Excellence 2186 „The Fuel Science Center" (grant ID: 390919832). The 600 MHz NMR spectrometer was funded by BMBF project SABLE (grant 03EK3543).

References

Abbott, T. M., Buchanan, G. W., Kruus, P., and Lee, K. C.: ^{13}C nuclear magnetic resonance and Raman investigations of aqueous carbon dioxide systems, Canadian Journal of Chemistry, 60, 1000–1006, https://doi.org/10.1139/v82-149, 1982.

Albert, K., Dreher, E.-L., Straub, H., and Rieker, A.: Monitoring electrochemical reactions by ^{13}C NMR spectroscopy, Magnetic Resonance in Chemistry, 25, 919–922, https://doi.org/10.1002/mrc.1260251017, 1987.

Bañares, M. A.: Operando methodology: combination of in situ spectroscopy and simultaneous activity measurements under catalytic reaction conditions, Catalysis Today, 100, 71–77, https://doi.org/10.1016/j.cattod.2004.12.017, 2005.

Bain, A. D. and Cramer, J. A.: Optimal NMR measurements for slow exchange in two-site and three-site systems, The Journal of Physical Chemistry, 97, 2884–2887, https://doi.org/10.1021/j100114a010, 1993.

Baruch, M. F., Pander, J. E., White, J. L., and Bocarsly, A. B.: Mechanistic Insights into the Reduction of CO_2 on Tin Electrodes using in Situ ATR-IR Spectroscopy, ACS Catalysis, 5, 3148–3156, https://doi.org/10.1021/acscatal.5b00402, 2015.

Benders, S., Gomes, B. F., Carmo, M., Colnago, L. A., and Blümich, B.: *In-situ* MRI velocimetry of the magnetohydrodynamic effect in electrochemical cells, Journal of Magnetic Resonance, 312, 106 692, https://doi.org/10.1016/j.jmr.2020.106692, 2020.

Benke, G. and Gnot, W.: The electrochemical dissolution of platinum, Hydrometallurgy, 64, 205 – 218, https://doi.org/10.1016/S0304-386X(02)00044-0, 2002.

Bonzel, H. P.: Alkali-metal-affected adsorption of molecules on metal surfaces, Surface Science Reports, 8, 43–125, https://doi.org/10.1016/0167-5729(88)90007-6, 1988.

Britton, M. M.: Magnetic Resonance Imaging of Electrochemical Cells Containing Bulk Metal, ChemPhysChem, 15, 1731–1736, https://doi.org/10.1002/cphc.201400083, 2014.

Britton, M. M., Bayley, P. M., Howlett, P. C., Davenport, A. J., and Forsyth, M.: In Situ, Real-Time Visualization of Electrochemistry Using Magnetic Resonance Imaging, The Journal of Physical Chemistry Letters, 4, 3019–3023, https://doi.org/10.1021/jz401415a, 2013.

Bundesnetzagentur: Frequenzplan, 2019.

Bussy, U. and Boujtita, M.: Review of advances in coupling electrochemistry and liquid state NMR, Talanta, 136, 155–60, https://doi.org/10.1016/j.talanta.2014.08.033, 2015.

Bussy, U., Giraudeau, P., Silvestre, V., Jaunet-Lahary, T., Ferchaud-Roucher, V., Krempf, M., Akoka, S., Tea, I., and Boujtita, M.: In situ NMR spectroelectrochemistry for the structure elucidation of unstable intermediate metabolites, Anal Bioanal Chem, 405, 5817–24, https://doi.org/DOI 10.1007/s00216-013-6977-z, 2013.

Carr, H. Y. and Purcell, E. M.: Effects of Diffusion on Free Precession in Nuclear Magnetic Resonance Experiments, Phys. Rev., 94, 630–638, https://doi.org/10.1103/PhysRev.94.630, 1954.

Falck, D. and Niessen, W. M. A.: Solution-phase electrochemistry-nuclear magnetic resonance of small organic molecules, TrAC Trends in Analytical Chemistry, 70, 31–39, https://doi.org/10.1016/j.trac.2015.03.010, 2015.

Falck, D., Oosthoek-de Vries, A. J., Kolkman, A., Lingeman, H., Honing, M., Wijmenga, S. S., Kentgens, A. P., and Niessen, W. M.: EC-SPE-stripline-NMR analysis of reactive products: a feasibility study, Anal Bioanal Chem, 405, 6711–20, https://doi.org/10.1007/s00216-013-7158-9, 2013.

Grisham, C. M. and Garrett, R. H.: Biochemistry, Cengage Learning, Boston, USA, 4 edn., 2010.

Grundmann, R.: Climate change as a wicked social problem, Nature geoscience, 9, 562–563, 2016.

Haas, T., Krause, R., Weber, R., Demler, M., and Schmid, G.: Technical photosynthesis involving CO_2 electrolysis and fermentation, Nature Catalysis, 1, 32–39, https://doi.org/10.1038/s41929-017-0005-1, 2018.

Hansen, J., Sato, M., Kharecha, P., Beerling, D., Berner, R., Masson-Delmotte, V., Pagani, M., Raymo, M., Royer, D. L., and Zachos, J. C.: Target Atmospheric CO: Where Should Humanity Aim?, The Open Atmospheric Science Journal, 2, 217–231, https://doi.org/10.2174/1874282300802010217, 2008.

Hargreaves, B. A., Worters, P. W., Pauly, K. B., Pauly, J. M., Koch, K. M., and Gold, G. E.: Metal-induced artifacts in MRI, AJR Am J Roentgenol, 197, 547–55, https://doi.org/10.2214/AJR.11.7364, 2011.

Hasbullah, R., Gardjito, Syarief, A. M., and Akinaga, T.: Gas Permeability Characteristics of Plastic Films for Packaging of Fresh Produce, Nogyo Shisetsu (Journal of the Society of Agricultural Structures, Japan), 31, 79–86, https://doi.org/10.11449/sasj1971.31.79, 2000.

Hatsukade, T., Kuhl, K. P., Cave, E. R., Abram, D. N., and Jaramillo, T. F.: Insights into the electrocatalytic reduction of CO(2) on metallic silver surfaces, Phys Chem Chem Phys, 16, 13 814–9, https://doi.org/10.1039/c4cp00692e, 2014.

Hernández, S., Amin Farkhondehfal, M., Sastre, F., Makkee, M., Saracco, G., and Russo, N.: Syngas production from electrochemical reduction of CO_2: current status and prospective implementation, Green Chemistry, 19, 2326–2346, https://doi.org/10.1039/c7gc00398f, 2017.

Hori, Y.: Electrochemical CO_2 Reduction on Metal Electrodes, Modern Aspects of Electrochemistry, Springer, New York, 42 edn., 2008.

Hori, Y., Murata, A., Kikuchi, K., and Suzuki, S.: Electrochemical reduction of carbon dioxides to carbon monoxide at a gold electrode in aqueous potassium hydrogen carbonate, Journal of the Chemical Society, Chemical Communications, https://doi.org/10.1039/C39870000728, 1987.

Hsieh, Y.-C., Senanayake, S. D., Zhang, Y., Xu, W., and Polyansky, D. E.: Effect of Chloride Anions on the Synthesis and Enhanced Catalytic Activity of Silver Nanocoral Electrodes for CO_2 Electroreduction, ACS Catalysis, 5, 5349–5356, https://doi.org/10.1021/acscatal.5b01235, 2015.

Ilott, A. J., Chandrashekar, S., Klockner, A., Chang, H. J., Trease, N. M., Grey, C. P., Greengard, L., and Jerschow, A.: Visualizing skin effects in conductors with MRI: (7)Li MRI experiments and calculations, J Magn Reson, 245, 143–9, https://doi.org/10.1016/j.jmr.2014.06.013, 2014.

Inzelt, G.: Pseudo-reference Electrodes, pp. 331–332, Springer Berlin Heidelberg, Berlin, Heidelberg, https://doi.org/10.1007/978-3-642-36188-3_14, 2013.

Jhong, H. R., Ma, S. C., and Kenis, P. J. A.: Electrochemical conversion of CO_2 to useful chemicals: current status, remaining challenges, and future opportunities, Current Opinion in Chemical Engineering, 2, 191–199, https://doi.org/10.1016/j.coche.2013.03.005, 2013.

Jungmann, P. M., Agten, C. A., Pfirrmann, C. W., and Sutter, R.: Advances in MRI around metal, Journal of Magnetic Resonance Imaging, 46, 972–991, https://doi.org/10.1002/jmri.25708, 2017.

Klod, S., Ziegs, F., and Dunsch, L.: In Situ NMR Spectroelectrochemistry of Higher Sensitivity by Large Scale Electrodes, Analytical Chemistry, 81, 10 262–10 267, https://doi.org/10.1021/ac901641m, 2009.

Kortlever, R., Shen, J., Schouten, K. J., Calle-Vallejo, F., and Koper, M. T.: Catalysts and Reaction Pathways for the Electrochemical Reduction of Carbon Dioxide, J Phys Chem Lett, 6, 4073–82, https://doi.org/10.1021/acs.jpclett.5b01559, 2015.

Liger-Belair, G., Prost, E., Parmentier, M., Jeandet, P., and Nuzillard, J.-M.: Diffusion Coefficient of CO_2 Molecules as Determined by ^{13}C NMR in Various Carbonated Beverages, Journal of Agricultural and Food Chemistry, 51, 7560–7563, https://doi.org/10.1021/jf034693p, 2003.

Lindskog, S.: Structure and mechanism of carbonic anhydrase, Pharmacology & Therapeutics, 74, 1–20, https://doi.org/10.1016/S0163-7258(96)00198-2, 1997.

Lu, Q., Rosen, J., Zhou, Y., Hutchings, G. S., Kimmel, Y. C., Chen, J. G., and Jiao, F.: A selective and efficient electrocatalyst for carbon dioxide reduction, Nat Commun, 5, 3242, https://doi.org/10.1038/ncomms4242, 2014.

525 Mairanovsky, V. G., Yusefovich, L. Y., and Filippova, T. M.: NMR-electrolysis combined method (NMREL). Basic principles and some applications, Journal of Magnetic Resonance (1969), 54, 19–35, https://doi.org/10.1016/0022-2364(83)90142-7, 1983.

Mani, F., Peruzzini, M., and Stoppioni, P.: CO_2 absorption by aqueous NH3 solutions: speciation of ammonium carbamate, bicarbonate and carbonate by a ^{13}C NMR study, Green Chemistry, 8, https://doi.org/10.1039/B602051H, 2006.

Meiboom, S. and Gill, D.: Modified spin-echo method for measuring nuclear relaxation times, Review of scientific instruments, 29, 688–691,
530 1958.

Mendonca, A. C., Malfreyt, P., and Padua, A. A.: Interactions and Ordering of Ionic Liquids at a Metal Surface, J Chem Theory Comput, 8, 3348–55, https://doi.org/10.1021/ct300452u, 2012.

Mincey, D. W., Popovich, M. J., Faustino, P. J., Hurst, M. M., and Caruso, J. A.: Monitoring of electrochemical reactions by nuclear magnetic resonance spectrometry, Analytical Chemistry, 62, 1197–1200, https://doi.org/10.1021/ac00210a020, 1990.

535 Moret, S., Dyson, P. J., and Laurenczy, G.: Direct, in situ determination of pH and solute concentrations in formic acid dehydrogenation and CO(2) hydrogenation in pressurised aqueous solutions using (1)H and (13)C NMR spectroscopy, Dalton Trans, 42, 4353–6, https://doi.org/10.1039/c3dt00081H, 2013.

Neukermans, S., Samanipour, M., Vincent Ching, H. Y., Hereijgers, J., Van Doorslaer, S., Hubin, A., and Breugelmans, T.: A Versatile In-Situ Electron Paramagnetic Resonance Spectro-electrochemical Approach for Electrocatalyst Research, ChemElectroChem, 7, 4578–
540 4586, https://doi.org/10.1002/celc.202001193, 2020.

Nunes, L. M., Moraes, T. B., Barbosa, L. L., Mazo, L. H., and Colnago, L. A.: Monitoring electrochemical reactions in situ using steady-state free precession ^{13}C NMR spectroscopy, Analytica Chimica Acta, 850, 1–5, https://doi.org/10.1016/j.aca.2014.05.022, 2014.

Prenzler, P. D., Bramley, R., Downing, S. R., and Heath, G. A.: High-field NMR spectroelectrochemistry of spinning solutions: simultaneous in situ detection of electrogenerated species in a standard probe under potentiostatic control, Electrochemistry Communications, 2, 516–
545 521, https://doi.org/Doi 10.1016/S1388-2481(00)00042-4, 2000.

Richards, J. A. and Evans, D. H.: Flow cell for electrolysis within the probe of a nuclear magnetic resonance spectrometer, Analytical Chemistry, 47, 964–966, https://doi.org/10.1021/ac60356a016, 1975.

Romanenko, K., Forsyth, M., and O'Dell, L. A.: New opportunities for quantitative and time efficient 3D MRI of liquid and solid electrochemical cell components: Sectoral Fast Spin Echo and SPRITE, Journal of Magnetic Resonance, 248, 96–104,
550 https://doi.org/10.1016/j.jmr.2014.09.017, 2014.

Sander, R.: Compilation of Henry's law constants (version 4.0) for water as solvent, Atmospheric Chemistry and Physics, 15, 4399–4981, https://doi.org/10.5194/acp-15-4399-2015, 2015.

Seitz-Beywl, J., Poxleitner, M., Probst, M. M., and Heinzinger, K.: On the interaction of ions with a platinum metal surface, International Journal of Quantum Chemistry, 42, 1141–1147, https://doi.org/10.1002/qua.560420505, 1992.

555 Serša, I. and Mikac, U.: A study of MR signal reception from a model for a battery cell, Journal of Magnetic Resonance, 294, 7–15, https://doi.org/https://doi.org/10.1016/j.jmr.2018.06.013, https://www.sciencedirect.com/science/article/pii/S109078071830168X, 2018.

Shaka, A., Keeler, J., Frenkiel, T., and Freeman, R.: An improved sequence for broadband decoupling: WALTZ-16, Journal of Magnetic Resonance (1969), 52, 335 – 338, https://doi.org/10.1016/0022-2364(83)90207-X, 1983.

Simon, H., Melles, D., Jacquoilleot, S., Sanderson, P., Zazzeroni, R., and Karst, U.: Combination of electrochemistry and nuclear magnetic resonance spectroscopy for metabolism studies, Anal Chem, 84, 8777–82, https://doi.org/10.1021/ac302152a, 2012.

Stanisavljev, D., Begović, N., Žujović, Z., Vučelić, D., and Bačić, G.: H NMR Monitoring of Water Behavior during the Bray-Liebhafsky Oscillatory Reaction, The Journal of Physical Chemistry A, 102, 6883–6886, https://doi.org/10.1021/jp980803x, 1998.

Tenailleau, E. and Akoka, S.: Adiabatic 1H decoupling scheme for very accurate intensity measurements in 13C NMR, Journal of Magnetic Resonance, 185, 50 – 58, https://doi.org/10.1016/j.jmr.2006.11.007, 2007.

Webster, R. D.: In situ electrochemical-NMR spectroscopy. Reduction of aromatic halides, Anal Chem, 76, 1603–10, https://doi.org/10.1021/ac0351724, 2004.

Whipple, D. T. and Kenis, P. J. A.: Prospects of CO_2 Utilization via Direct Heterogeneous Electrochemical Reduction, The Journal of Physical Chemistry Letters, 1, 3451–3458, https://doi.org/10.1021/jz1012627, 2010.

Williamson, N. H., Dower, A. M., Codd, S. L., Broadbent, A. L., Gross, D., and Seymour, J. D.: Glass Dynamics and Domain Size in a Solvent-Polymer Weak Gel Measured by Multidimensional Magnetic Resonance Relaxometry and Diffusometry, Phys. Rev. Lett., 122, 068 001, https://doi.org/10.1103/PhysRevLett.122.068001, 2019.

Zhang, X. and Zwanziger, J. W.: Design and applications of an in situ electrochemical NMR cell, J Magn Reson, 208, 136–47, https://doi.org/10.1016/j.jmr.2010.10.013, 2011.

Zhu, D. D., Liu, J. L., and Qiao, S. Z.: Recent Advances in Inorganic Heterogeneous Electrocatalysts for Reduction of Carbon Dioxide, Advanced Materials, 28, 3423–52, https://doi.org/10.1002/adma.201504766, 2016.